Improving Gr/SiO Negative Electrode Formulations: Effect of Active Material, Binders, and Single-Walled Carbon Nanotubes

Andreas Röck, Margret Wohlfahrt-Mehrens, Peter Axmann, and Alice Hoffmann*

With the growing demand for high-energy-density lithium-ion batteries, silicon oxide (SiO) has emerged as a promising anode material due to its high specific capacity. However, its use entails high irreversible losses and mechanical stress. Pre-lithiated SiO (Li-SiO) blended with graphite enables electrodes with rather low irreversible losses, high specific capacity, and less mechanical stress. However, so far, insights about processing Li-SiO are missing in literature. This work deals with Gr/SiO negative electrodes containing 20 wt% SiO in the active mass. We investigate the effects of different suspension formulations on their rheological properties and the electrochemical performance of the electrodes. Our findings prove superior electrochemical properties of anodes made from Li-SiO compared to pristine SiO. However, we show that the basicity of suspensions containing Li-SiO causes challenges for their processability. The integration of single-walled carbon nanotubes is shown to be essential for counteracting the adverse effects and enabling electrodes with enhanced adhesion, reduced irreversible losses, and stable cycling. A good cell performance is demonstrated with electrodes containing as much as 96.8% of active mass. Our findings provide essential insights into the correlation between formulation, processability, and electrochemical performance of Gr/SiO blends, supporting the development of industrial-scale production processes.

1. Introduction

Lithium-ion batteries (LIBs) have become a cornerstone in today's electrical energy storage, widely employed in portable electronics, electric vehicles, and renewable energy storage. As demand for higher energy density increases, researchers have been seeking alternatives to conventional graphite anodes. One of the most promising active materials is silicon, which has a significantly higher theoretical specific capacity than graphite. Fully lithiated silicon ($Li_{22}Si_5$)[1] has a capacity of 4212 mAh g^{-1} compared to 372 mAh g^{-1} for graphite (LiC$_6$).[2] However, its practical application has been hindered so far by severe volumetric changes (up to 400%)[3] during lithium-ion insertion and extraction (lithiation/delithiation). These structural transformations lead to mechanical degradation of the electrodes as well as rapid capacity fading and a short cycle life of the battery cells.[4]

A. Röck, A. Hoffmann
Zentrum für Sonnenenergie- und Wasserstoff-Forschung Baden-Württemberg (ZSW)
Akkumulatoren Materialforschung (ECM)
Lise-Meitner-Straße 24, 89081 Ulm, Germany
E-mail: alice.hoffmann@zsw-bw.de

M. Wohlfahrt-Mehrens, P. Axmann
Zentrum für Sonnenenergie- und Wasserstoff-Forschung Baden-Württemberg (ZSW)
Akkumulatoren Materialforschung (ECM)
Helmholtzstraße 8, 89081 Ulm, Germany

SiO$_x$ with $x \approx 1$ (referred to as SiO hereafter) offers a compromise between the high capacity of elemental silicon and greater stability due to its reduced volume expansion (120%),[5,6] making it a promising alternative active material for LIB anodes.[7] However, its primary drawback lies in the irreversible formation of lithium silicate (Li_4SiO_4)[8] during the first lithiation, which leads to significant irreversible capacity losses and low initial coulombic efficiency (ICE) of around 70% or less.[6,9,10] Moreover, achieving sufficient cycling stability with pure SiO electrodes remains a challenge for practical applications. To address these issues, blending SiO with graphite has become a viable approach, allowing for the exploitation of SiO's high capacity while maintaining sufficient long-term stability.[11,12] Current state-of-the-art negative electrodes in consumer cells typically contain around 5 wt% SiO, with the goal of increasing its share to 20% or more in future formulations.[9,13] However, to realize this, the challenge of high irreversible losses must firstly be addressed.[13] Prelithiation has emerged as a promising strategy to tackle this issue by generating Li_4SiO_4 from SiO in a dedicated ex-site process before assembling the battery cells,[9] thereby compensating for the initial capacity losses and making SiO more competitive with conventional graphite anodes. Among the various prelithiation strategies, such as electrochemical prelithiation[14] or the incorporation of stabilized lithium metal powder,[15] one of the most promising approaches is the use of lithium-doped SiO (Li–SiO) combined with a carbon coating on the SiO particles. This method not only significantly enhances the ICE to over 90%[6,9] but also allows for the use of aqueous electrode preparation methods, enabling the direct adoption of existing manufacturing processes.[6] In addition, Li–SiO still provides a reversible capacity of $\approx$1400 mAh g^{-1},[6,9] making it a highly attractive candidate for next-generation LIB anodes.

An LIB anode consists of active materials, binders, and conductive additives. Typical formulations of water-based electrode suspensions contain less than 5 wt% binder, with the state-of-the-art binder system being a combination of sodium carboxymethyl cellulose (CMC) and styrene-butadiene rubber (SBR).[16] CMC provides a suitable rheological suspension properties for the coating process, while SBR ensures the flexibility and adhesion of the resulting electrode.[17] To enhance the electronic conductivity of the electrode composite, carbon black (CB) is added.[18] Another promising conductive additive is single-walled carbon nanotubes (SWCNTs), which have shown considerable potential in improving the stability and overall performance of SiO-based electrodes.[11,12,19–21] SWCNTs are highly effective in improving electronic conductivity and enabling a more efficient charge transport within the electrode structure.[19] Moreover, their unique mechanical properties help reinforce the structural integrity of the electrode, mitigating mechanical degradation and improving cycling stability during repeated lithiation and delithiation.[20] Despite these advantages, the influence of SWCNTs on the rheological properties of LIB electrode suspensions remains mostly unexplored. Rheological characteristics, such as suspension viscosity and structural strength, play a crucial role in electrode manufacturing and coating processes.[22]

Previous research has explored pristine SiO (p-SiO) in terms of binders and electrode composition.[23,24] Sufficient cycling stability has also been achieved in some studies.[24] However, detailed research on improving electrode formulations with Li–SiO remains limited. Addressing this gap is crucial for advancing the practical application of Li–SiO in LIBs. Recent studies have begun to explore this material more closely regarding its structural and electrochemical behavior.[6,9] For instance, a fundamental study by Hirose et al.[9] provided a significant insights into the phase and structural changes occurring in Li–SiO compared to p-SiO, offering a deeper understanding of the material's transformation during cycling. The electrodes studied contained a high Li–SiO content of 20% with a state-of-the-art active material content of 95.6%. However, Hirose et al.'s work was focused on the fundamental properties of Li–SiO. Practical requirements on electrode formulation or processing conditions were not elucidated.

Similarly, Reynier et al.[6] explored the practical implementation of Li–SiO in LIBs, investigating cells with up to 20% Li–SiO content in both pouch and cylindrical formats. Their study provided valuable insights into the electrochemical performance of Li–SiO in large-format cells. However, it focused primarily on cell performance rather than elucidating the electrode formulation and suspension preparation processes. Furthermore, the active material content in their suspensions was only 91%, while industrial requirements usually demand at least 94%. Additionally, rheological data of the suspensions, which are important for large-scale electrode production, were not included. Despite the advancements made with Li–SiO, further improvements are needed to fully meet industrial standards. As described, formulations for this system are yet under-researched, particularly regarding the requirements posed by large-scale processing.

Our study addresses these research gaps. To the best of our knowledge, it is the first work that explores the impact of the application of Li–SiO in highly relevant LIB electrode formulations on the processability in the electrode production process and analyzes the electrochemical properties of the associated electrodes in half-cells and full-cells.

We present recent advancements in electrode formulation, particularly focusing on anode compositions with a high Li–SiO content (20% of the active material) and a total active mass content of up to 96.8%. We will show that the fundamental properties of the suspensions are strongly negatively affected by replacing p-SiO with Li–SiO, which restricts their industrial application. To address this limitation, we explore the implementation of SWCNTs and the role of SBR functionalization. The influence of the use of Li–SiO and the type of formulation on the rheological properties of the water-based anode suspensions is investigated, the implications on their processability are elucidated, and the challenges arising for an industrial process are explained. It will be shown that the properties determining the industrial processability of the Li–SiO-containing suspensions can be substantially improved by the formulation. Moreover, we evaluate the impact of the formulations on the characteristic values of the formation and the rate capability of half-cells and full-cells from the corresponding electrodes, and we attribute the internal resistance and cycling stability of full-cells containing these electrodes. By providing and correlating these detailed insights, our work contributes to the practical development of electrode manufacturing with industrial processes. Importantly, all materials used in this study are commercially available in industry-relevant quantity, underscoring the real-world applicability and relevance of our findings for next-generation LIB production.

2. Experimental Section

p-SiO and Li–SiO with a carbon coating (KSC-1265, KSC-7144, Shin-Etsu) and graphite (SMG-A5, Showa Denko) were utilized as active materials, with mean particle sizes of 7, 8, and 18 µm, respectively, in an 80:20 (graphite to SiO) weight ratio. CB (Super C65, Imerys) and an aqueous dispersion of SWCNTs (TUBALL BATT H$_2$O 0.4, OCSiAl) were employed as conductive additives. CMC (Sunrose MAC500LC, Nippon Paper) and SBR (BM451-B, Zeon and Licity 2698, BASF SE) served as a binders. The weight ratio of CMC to SBR was 1:1. All materials were used as received without further modification.

2.1. Preparation of the Pilot-Scale Cathode

The suspension for the pilot-scale cathode consisted of 92% lithium iron phosphate LiFePO$_4$ (LFP) (Epsilon CAM GmbH), 4% polyvinylidene fluoride (PVdF) (Solvay Solexis), 3% CB (Super C65, Imerys), and 1% graphite (SFG6L, Imerys) and was mixed in a 10 L planetary mixer (Netzsch) with N-methyl-2-pyrrolidon (NMP) as a solvent. The electrode suspension was then applied with a comma bar on an aluminum foil (15 µm) using a pilot-scale coater (LACOM) equipped with four different drying zones (2 m each). The mass loading of the electrode was 17 mg cm^{-2} per side, resulting in an areal capacity of 2.5 mAh cm^{-2}. Finally, the

electrode was calendered, and the density of the composite was 2.0 g cm^{-3}.

2.2. Suspension Preparation

The preparation of the suspensions at lab scale was performed in a double-walled dissolver mixer (VMA-Getzmann DISPERMAT) equipped with a 250 mL vessel and a 40 mm dissolver disc. The temperature of the mixtures was maintained at 20 °C during mixing. The rotational speed during each step was adjusted until a stable vortex, also known as the donut effect,[25] was established. Correspondingly, the rotational speeds provided in the following should be considered as reference values and were slightly varied between the experiments. The first step of the mixing procedure involved preparing a CMC solution by adding CMC powder to water as the solvent and stirring the mixture at 1500 rpm for 15 min until it became clear. For suspensions containing CB, the CB was added in the subsequent step and dispersed in the CMC solution for 15 min at 1700 rpm. When SWCNTs were included in the formulation, an SWCNT suspension was added to either the CB suspension or the CMC solution, and the mixture was then stirred together for 5 min at 1500 rpm. In the following step, the active materials were added, first the SiO and then the graphite powder. The mixture was stirred for 20 min at a rotational speed of 1700 rpm. At last, the suspensions were completed by adding the SBR at 750 rpm, considering the shear sensitivity of the SBR, and stirred for 15 min. The final solid content of the suspensions was targeted to be 44.5 wt%. The concentration of the initial CMC solution varied between 1.6 and 2 wt%, depending on the use of SWCNT suspension, to consider that this introduced additional water into the system. The investigated formulations are summarized in **Table 1**. The nomenclature of the electrodes provides detailed information about their formulation. The leading letter indicates whether functionalized (f) or nonfunctionalized (n) SBR was used, while the following index represents the total binder content (CMC + SBR) in wt%. The letters "CB," followed by an index, denote the CB content in wt%. Finally, the SWCNT content is indicated by "CNT" and its respective index, with "01" signifying a 0.1 wt% addition of SWCNTs to the electrode formulation. The use of p-SiO is indicated by a leading "p."

2.3. Rheological Measurements

The rheological properties of the electrode suspensions were determined using an Anton Paar rheometer (Physica MCR101) with a 50 mm cone-plate geometry (1° angle, sample volume 0.6 mL). To prevent errors caused by solvent evaporation, a solvent trap[26] was employed for all experiments. The viscosity curves were obtained through measurements in rotational mode, utilizing a logarithmic ramp starting at a shear rate of 0.1 s^{-1} and ending at a shear rate of 1000 s^{-1}. Five points per decade were measured. No fixed duration of each measurement at each shear rate was specified in order to avoid transient effects in the low shear rate range.[27]

Amplitude sweep experiments were conducted to ascertain the linear viscoelastic region of the suspensions. The experiments involved applying a constant angular frequency of 10 rad s^{-1} while incrementally increasing the amplitude of deformation from 0.05 to 500% (four measurements per decade). Subsequently, the maximum deformation amplitude within the linear viscoelastic region was determined, corresponding to a 3% deviation from the linear response, and frequency sweep experiments were conducted. These measurements involved keeping the deformation amplitude (inside the linear viscoelastic region) constant while varying the frequency of the oscillatory movement. The experiments commenced at an angular frequency of 628.32 rad s^{-1} (100 Hz) and concluded at 0.1 rad s^{-1}.

2.4. pH Measurements

The pH of the electrode suspensions was determined by using a pH meter (Metrohm 913), which was calibrated before each measurement. After mixing, 20 mL of the suspensions was extracted from the mixing vessel and transferred to a separate container, where the pH electrode was immersed. The measurements were conducted at a temperature of 20 °C.

2.5. Electrodes Fabrication

The electrode suspensions were cast on 10 μm thick battery-grade copper foil (JX Nippon) using the doctor blade (elcometer) technique. Depending on the active material content, the target mass loading was ≈6 mg cm^{-2}, corresponding to an areal capacity of 3 mAh cm^{-2}. Subsequently, the wet films were dried on a hot plate at 40 °C for 1 h, followed by 1 h at 60 °C. The composites were then compacted to a target density ranging between 1.0 and 1.1 g cm^{-3} by using a lab-scale calendering machine (Sumet Technologies). The electrode thickness for calculating the density was determined using a digital micrometer screw (Mitutoyo).

2.6. Adhesion Measurements

The z-direction tensile strength of the coatings on the current collector foil was determined using a ZwickRoell Z2.5 device. Two compression plates covered with double-sided adhesive tape (3 M) were utilized for the test. The electrodes were attached

Table 1. Summary of the formulations of the investigated electrodes.

Electrode	SiO	SBR	AM [wt%]	Binder [wt%]	CB [wt%]	SWCNTs [wt%]
p-f$_4$CB$_0$CNT$_{01}$	p-SiO	Licity	95.8	4	0	0.1
n$_4$CB$_2$CNT$_0$	Li–SiO	Zeon	94	4	2	0
f$_4$CB$_2$CNT$_0$	Li–SiO	Licity	94	4	2	0
f$_4$CB$_1$CNT$_{01}$	Li–SiO	Licity	94.8	4	1	0.1
f$_4$CB$_0$CNT$_{01}$	Li–SiO	Licity	95.8	4	0	0.1
f$_3$CB$_0$CNT$_{01}$	Li–SiO	Licity	96.8	3	0	0.1
n$_4$CB$_0$CNT$_{01}$	Li–SiO	Zeon	95.8	4	0	0.1

Batteries & Supercaps

Research Article
doi.org/10.1002/batt.202400764

![Chemistry Europe logo] Chemistry Europe
European Chemical
Societies Publishing

to the tape on the lower plate. During the measurement, the upper plate was pressed with a force of 2 kN for 120 s on the electrode. Then, the plates were detached in the z-direction at a controlled speed of 1000 mm min^{-1} with the tensile force being recorded at a data acquisition rate of 500 Hz. Three to five samples per electrode were analyzed, and the average tensile strength along with the standard deviation was calculated. Further details on the measurement setup can be found in the study by Haselrieder et al.[28]

2.7. Electrochemical Measurements in Half-Cells

For the half-cell measurements, circular electrodes with 18 mm diameter (2.54 cm^2) were punched out, weighted, and dried overnight under vacuum ($p \approx 10^{-3}$ mbar) at a temperature of 130 °C. Subsequently, in an argon-filled glovebox (MBRAUN), they were assembled into half-cells with a Li-reference electrode (EL-Cell), an 18 mm Li counter electrode (PI-KEM), and two layers of glass fiber separator (Whatman GF/A). A 175 μL of electrolyte, consisting of 1 M LiPF$_6$ in EC/DEC (3/7 wt) with 10% FEC, was added to the cells. After assembly, the cells rested for 6 h to allow the electrolyte to impregnate the electrodes and the separator.

The half-cell measurements were conducted at room temperature using a BioLogic VMP 3. The potential of the working electrode was controlled within the potential range of 1.5–0.01 V relative to the Li reference electrode. The formation process consisted of three consecutive cycles at a current corresponding to 0.1C. Lithiation was performed using a constant current (CC) phase, followed by a constant voltage (CV) phase at 0.01 V. The CV phase was terminated as soon as the current dropped below a value corresponding to 0.01C. Delithiation was performed using a CC only. After this formation process, a rate capability test was performed, beginning with the investigation of delithiation capacities. Lithiation was consistently carried out at a current density of 1 mA cm^{-2}, which corresponds to ≈0.3C, followed by a CV phase at 0.01 V (0.01C as cutoff). Delithiation was then examined with current densities of 0.25, 0.5, 2.5, 5, and 10 mA cm^{-2}. Three cycles with each current density were carried out. Similarly, during the subsequent lithiation rate test, delithiation was conducted at a CC density of 1 mA cm^{-2}, while the lithiation current density was increased every three cycles. The investigated current densities were again 0.25, 0.5, 2.5, 5, and 10 mA cm^{-2}. No CV phase was applied during this test.

2.8. Electrochemical Measurements in Pouch Cells

For the electrochemical characterization in full-cells, bilayer pouch cells were assembled using double-side coated LFP cathodes from the pilot line of our institute as counter electrodes and two single-side coated anodes from the experiments described in this article. A minimum of three cells were assembled for each investigated anode. The cathodes and anodes were cut to areas of 23.94–26 cm^2, respectively, and dried under vacuum for 9 h at 130 °C. Next, an electrode stack was prepared by arranging a cathode in the middle and two anodes on the outer sides with Celgard 2325 separators between them using an automated

stacking machine (Homburger). Current collector tabs were then ultrasonically welded to the electrodes and the stack was inserted in a pouch bag and sealed. The pouch cell assembly was conducted in a dry room with a dew point below −60 °C. After further drying at 80 °C under vacuum for 16 h, the pouch bags were transferred into an argon-filled glovebox (MBRAUN). Here, they were filled with 900 μL of electrolyte (1 M LiPF$_6$ in EC/DEC (3/7 wt) with 10% FEC) and sealed. Before commencing the formation process, the cells were stored for 12 h to ensure complete soaking of the electrolyte.

The electrochemical tests were conducted at room temperature using a BaSyTec cell test system (BaSyTec CTS). The voltage range employed was 2.0–3.6 V, with charging consistently carried out using a CC, followed by a CV phase (0.2C as cutoff). Discharge steps were executed using the CC only. The formation process comprised three cycles of charging and discharging at 0.1C. After formation, the discharge rate capability was investigated by charging the cells with 1 mA cm^{-2} and increasing the discharge current density every three cycles. The applied current densities were 0.25, 0.5, 2.5, 5, 10, 15, and 20 mA cm^{-2}. Similarly, the charge rate capability was examined by discharging the cells with 1 mA cm^{-2} and increasing the charge current density every three cycles. The applied charge current densities were 0.25, 0.5, 2.5, 5, 10, and 15 mA cm^{-2}. For the evaluation of the charge rate capability, only the CC step was considered. After the rate capability test, a cycling stability test was performed by applying 0.5C charge and 1C discharge. During the test, every 50th cycle was designated as a check-up cycle, involving a direct current internal resistance (DCIR) measurement. Within these cycles, the actual discharge capacity was measured by the BaSyTec system, and the cells were subsequently discharged to a 50% state of charge (SoC). At this SoC, the cells were allowed to relax for 60 min to determine the open circuit voltage, after which a 2C charge pulse was applied for 18 s. Following the pulse, the cells relaxed again for 10 min before a 2C discharge pulse was applied for 18 s. To calculate the internal resistance, the voltage drop after 10 s of discharge was divided by the applied current, in accordance with the Ohm's law. The checkup cycles are omitted from the diagrams for clarity. The resistance increase during the rate capability test has also been determined using the DCIR method under the same conditions.

3. Results and Discussion

The formulation of electrodes for LIB is crucial not only for enhancing electrochemical performance and cycling stability but also for ensuring the processability of the electrode suspension on a larger scale. In this study, we examine the influence of prelithiated SiO particles on the rheological properties of battery electrode suspensions and their impact on the electrochemical properties of the resulting electrodes in half and full-cells. Additionally, we investigate the effects of the use of functionalized SBR as a binder, compared to a nonfunctionalized SBR. Furthermore, we introduce SWCNTs as a conductive additive and explore their multifunctional role in rheological suspension properties, mechanical electrode properties, and electrochemical cell properties.

Batteries & Supercaps

Research Article
doi.org/10.1002/batt.202400764

Chemistry Europe
European Chemical
Societies Publishing

Each electrode formulation was evaluated following a systematic approach as listed here. First, the impact of the formulation on the rheological properties of the suspensions was assessed. After casting the suspensions onto copper foil, followed by drying and calendering, the adhesive strength of the electrode composites on the copper foil was measured. Following the mechanical characterization, the electrochemical properties were examined through half-cell measurements with a lithium reference electrode, including formation and a rate capability test. After gaining insights into the electrochemical properties of the electrodes in half-cells, further measurements were conducted in full pouch cells to assess their behavior under more practical, application-relevant conditions. The tests in full-cells included formation, a rate capability test, and a cycling stability test in a complete battery setup.

Rheological measurements are a powerful tool for predicting the behavior during coating. By using measurements in rotational mode, the viscosity η of a sample can be determined as related to the shear rate resulting in a viscosity curve.[29] The viscosity η is defined as the ratio between shear stress τ and shear rate $\dot{\gamma}$, as shown in Equation (1), and serves as a measure of a sample's resistance to flow.[30]

$$\eta = \frac{\tau}{\dot{\gamma}} \tag{1}$$

The shear rate $\dot{\gamma}$ is defined as the velocity v within the shear field divided by the height h of the film layer, as described in Equation (2).

$$\dot{\gamma} = \frac{v}{h} \tag{2}$$

For battery-electrode suspensions, non-Newtonian and particularly shear-thinning behavior is expected, where viscosity decreases gradually with increasing shear rate. This behavior is crucial for the coating process because the electrode suspension must flow with minimal resistance under high shear rates, such as those present in a slot-die. Simultaneously, the viscosity at rest should be high to ensure suspension stability and a homogeneous wet layer without sagging. Rheological measurements can also be conducted in oscillatory mode, where a sinusoidal input is applied to the sample and the resulting response is recorded. Battery electrode suspensions typically exhibit viscoelastic properties, leading to a time lag in the response. This time lag is characterized by the phase shift angle δ, which describes the phase difference between the input and the response. Additionally, oscillatory measurements provide the complex shear modulus G^*, which is a measure of the material's rigidity and can be used to characterize the sample's state.[31] The complex modulus G^* can be separated into its real part, the storage modulus (G'), and its imaginary part, the loss modulus (G''), according to Equation (3) and (4).[30,32]

$$\text{Re}(G^*) = G' = G^* \cdot \cos \delta \tag{3}$$

$$\text{Im}(G^*) = G'' = G^* \cdot \sin \delta \tag{4}$$

The storage modulus G' represents the elastic portion of the material and is a measure for the deformation energy stored when the sample is sheared, which is fully recoverable upon redeformation. In contrast, the loss modulus G'' represents the viscous portion and is a measure of the deformation energy lost due to internal friction and heat generation.

The ratio between G' and G'' further characterizes the material's state. When G' exceeds G'', the sample predominantly exhibits gel-like behavior. Conversely, if the loss modulus G'' surpasses the storage modulus G', the material behaves more like a liquid. For a battery electrode suspension, gel-like behavior at rest is desirable, as it ensures stability against sedimentation during the coating process.

For our investigations, suspensions with the formulations shown in Table 1 have been prepared and applied to produce electrodes.

Table 2 presents the mechanical properties of these electrodes. The consistency in mass loadings and composite densities ensures the admissibility of comparing the electrochemical properties devoid of an influence by electrode design. The lower mass loading of the electrode with p-SiO compared to that of Li–SiO-based electrodes (5.22 compared to 6 mg cm^{-2}) is required to obtain a similar areal capacity due to the higher specific capacity of p-SiO. The adhesion values obtained from the z-direction tensile test show considerable variations, which is discussed in the following subsections.

It is worth noting that compared to state-of-the-art graphite electrodes, the composite densities of the investigated Gr/SiO electrodes are relatively lower. This deliberate choice of a lower target density was made to prevent the cracking of SiO particles, which often occurs with intense calendering and causes increased irreversible losses. Furthermore, the higher porosity associated with lower density aids in resisting the volume expansion of the SiO particles and contributes to a reduction in ionic pore resistance. As mentioned, the produced electrodes were characterized in half-cells. The measured ICE, the specific capacity, and the areal capacity are summarized in **Table 3**. Following formation, all electrodes exhibit similar areal capacities, ensuring the comparability of the results from their subsequent electrochemical characterization. The values presented in Table 3 are further discussed in detail in the corresponding subsection.

3.1. Comparison of p-SiO and Li–SiO

This section provides a comparative analysis of p-SiO and Li–SiO, focusing on their respective impacts on the stability and

Table 2. Mechanical properties of the investigated electrodes.

Electrode	Mass loading [mg cm^{-2}]	Density [g cm^{-3}]	Adhesion [N mm^{-2}]
p-f$_4$CB$_0$CNT$_{01}$	5.22	1.08	1.35 ± 0.18
n$_4$CB$_2$CNT$_0$	6.48	1.04	1.07 ± 0.02
f$_4$CB$_2$CNT$_0$	6.00	1.10	0.49 ± 0.14
f$_4$CB$_1$CNT$_{01}$	5.96	1.06	0.39 ± 0.04
f$_4$CB$_0$CNT$_{01}$	6.23	1.01	1.06 ± 0.12
f$_3$CB$_0$CNT$_{01}$	6.08	1.11	0.47 ± 0.08
n$_4$CB$_0$CNT$_{01}$	6.11	1.05	1.08 ± 0.14

Batteries & Supercaps

Research Article
doi.org/10.1002/batt.202400764

Chemistry Europe
European Chemical
Societies Publishing

Table 3. Results of the half-cell measurements after formation.

Electrode	ICE [%]	Specific capacity [mAh g^{-1}]	Areal capacity [mAh cm^{-2}]
p-f$_4$CB$_0$CNT$_{01}$	84.36	613.54	3.06
n$_4$CB$_2$CNT$_0$	93.07	555.06	3.38
f$_4$CB$_2$CNT$_0$	90.89	523.53	2.95
f$_4$CB$_1$CNT$_{01}$	91.94	571.81	3.21
f$_4$CB$_0$CNT$_{01}$	93.28	567.41	3.38
f$_3$CB$_0$CNT$_{01}$	93.44	568.72	3.32
n$_4$CB$_0$CNT$_{01}$	93.37	560.61	3.29

processability of the electrode suspensions, as well as their impact on the electrochemical properties of electrodes. For this purpose, two suspensions and electrodes were prepared in lab scale: one containing p-SiO (p-f$_4$CB$_0$CNT$_{01}$) and the other Li–SiO (f$_4$CB$_0$CNT$_{01}$), both utilizing functionalized SBR as a binder and SWCNTs as a conductive additive. Detailed information about the formulations can be found in Table 1.

The results of the rheological measurements are shown in **Figure 1**. The suspension consisting of prelithiated particles exhibited a notably (29%) lower viscosity of 56 Pa s compared to 79 Pa s for the suspension containing p-SiO at a shear rate of 1 s^{-1}. Additionally, the suspension containing p-SiO exhibited gel-like properties (G' > G'') across the entire frequency range, indicating a highly stable structure. In contrast, the suspension with Li–SiO particles demonstrated lower G' and G'' values, with predominantly liquid-like behavior (G' < G''), except in the low-frequency range, where a gel-like state was observed. However, even in this range, G' is lower by a factor of 2.5, indicating a considerably lower structural strength at rest for the electrode suspension containing Li–SiO. Consequently, the sedimentation stability of the suspension was significantly lower, which could present serious challenges for large-scale electrode production.

The significant differences in rheological properties can be attributed to the pH of the suspensions. While the suspension with p-SiO maintained a neutral pH of 7, the pH rose to 12.25 when Li–SiO was used instead. This substantial pH difference can be explained by the circumstance that prelithiated SiO particles induce a basic reaction during aqueous processing, as previously reported.[33] The different rheological properties of the

suspensions containing Li–SiO instead of p-SiO arise from the instability of CMC at high pH levels. According to the literature, CMC is stable within a pH range between 2 and 10,[34,35] which is significantly lower than the observed pH of 12.25 in the suspension containing Li–SiO. At high pH, unsubstituted cellulose blocks in the CMC chains become solubilized, weakening hydrophobic interactions. Consequently, the viscosity and structural strength of the CMC gel are significantly reduced.[34] Therefore, a strongly alkaline environment negatively affects the processability of CMC-based suspensions, as evidenced by our findings.

Table 2 presents the adhesive strength of the electrode composites on copper foil. The electrode containing p-SiO as the active material (p-f$_4$CB$_0$CNT$_{01}$) exhibited an adhesive strength of 1.35 N mm^{-2}, whereas the electrode with Li-SiO (f$_4$CB$_0$CNT$_{01}$) showed a 20% lower adhesive value of 1.06 N mm^{-2}.

Figure 2 illustrates the first formation cycle of the half-cells. In the case of p-SiO as the AM (p-f$_4$CB$_0$CNT$_{01}$), the potential curve clearly indicates higher irreversible losses. Additionally, Figure 2b shows that p-SiO exhibited a higher overpotential compared to Li–SiO during the initial lithiation. This suggests that, in addition to solid electrolyte interphase (SEI) formation, inactive species, such as Li$_4$SiO$_4$, were also formed.[36] In the case of Li–SiO (f$_4$CB$_0$CNT$_{01}$), these inactive species have been formed in advance,[9] thereby limiting its contribution to lithium consumption and increasing the coulombic efficiency of the first cycle.

Table 3 presents the corresponding measured values from the formation of the half-cells, a blend of 20% p-SiO and 80% graphite exhibited a specific capacity of 614 mAh g^{-1}, whereas a blend with Li-SiO had a specific capacity of 563 mAh g^{-1}. Nevertheless, the irreversible losses of the electrode with p-SiO were significantly higher (84% ICE). With Li–SiO as part of the active material, the irreversible losses were lower, resulting in an ICE exceeding 93%. While this discrepancy of the irreversible losses may be negligible in a half-cell with a quasiinfinite reservoir of lithium, it becomes crucial in a full-cell setup, where a considerable amount of lithium from the cathode is irreversibly lost during the first charge.

During the rate capability test of the half-cells, the electrode containing p-SiO (p-f$_4$CB$_0$CNT$_{01}$) demonstrated higher specific capacities compared to the electrode with Li–SiO (f$_4$CB$_0$CNT$_{01}$), as shown in **Figure 3**. Even at the highest current density of 10 mA cm^{-2}, the electrode with p-SiO has a specific
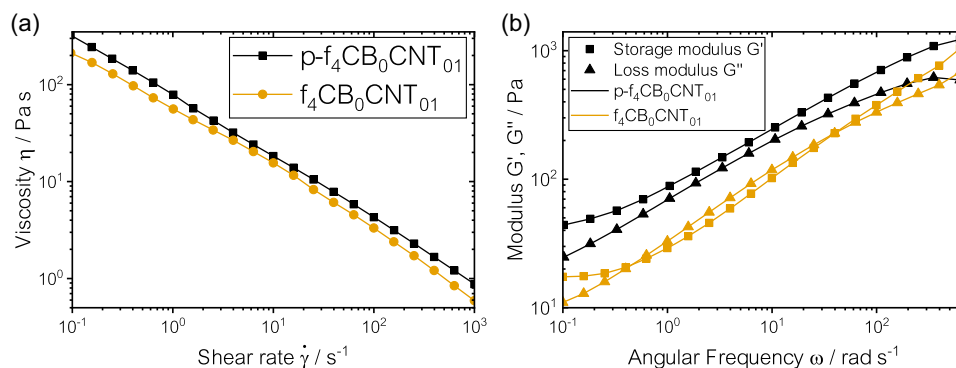

Figure 1. Rheological properties of the electrode suspensions containing either p-SiO or Li–SiO. a) Viscosity curves and b) frequency dependent behavior.
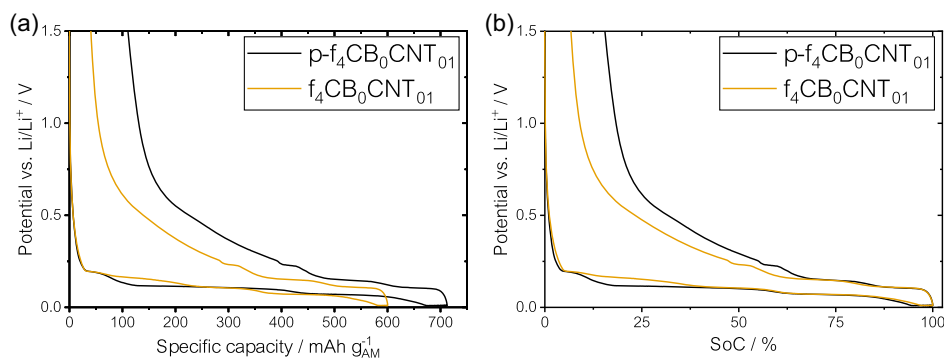
Figure 2. First formation cycle of half-cells with p-SiO (p-$f_4CB_0CNT_{01}$) and Li–SiO ($f_4CB_0CNT_{01}$): a) potential over specific capacity and b) potential over SoC.

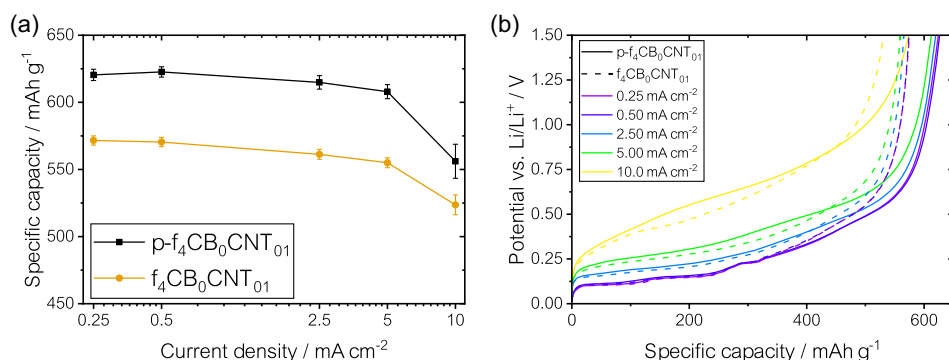**Figure 3.** Potential-controlled rate capability (delithiation) test of electrodes with p-SiO (p-$f_4CB_0CNT_{01}$) and Li–SiO ($f_4CB_0CNT_{01}$) conducted in half-cells; a) capacity over current density and b) potential curves at various current densities.

capacity of 556.1 mAh g^{-1}, which is nearly as high as the specific capacity of the electrode containing Li–SiO at low currents (571.6 mAh g^{-1}). In Figure 3b, the potential curves of both electrodes display nearly identical shapes in the range of low SoC, where the graphite component undergoes delithiation before the SiO. After ≈350 mAh g^{-1} at low current density, the curves begin to deviate, and higher specific capacities are reached with p-SiO. Notably, a lower polarization for the electrodes comprising Li–SiO is observed at higher current densities. This is noteworthy since the mass loading of those electrodes was 19% higher, and the reverse behavior would be expected. One possible explanation for this phenomenon could be an enhanced lithium-ion diffusivity within the prelithiated SiO particles, allowing the ions to move more efficiently through the particles, thereby improving the overall kinetics of the delithiation process.

Figure 4 shows the voltage profiles of the first and third formation cycle of the pouch cells, and in **Table 4**, the corresponding values can be found. Due to the irreversible lithium losses, the coulombic efficiency during the initial formation cycle was below 80% for cells with p-SiO-based anodes (p-$f_4CB_0CNT_{01}$). In comparison, with anodes containing Li–SiO ($f_4CB_0CNT_{01}$), this value reached nearly 91%, which can be seen from the voltage profiles of the first formation cycle (Figure 4a).
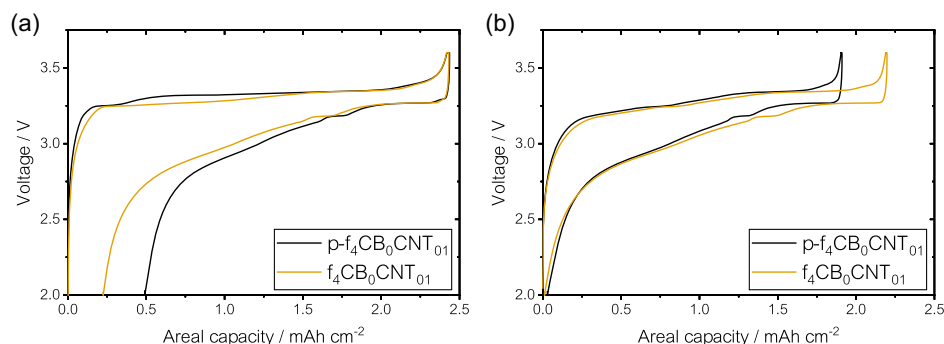

Figure 4. Voltage profiles of the formation of Gr/SiO‖LFP pouch cells with anodes containing p-SiO (p-$f_4CB_0CNT_{01}$) or Li-SiO ($f_4CB_0CNT_{01}$): a) first formation cycle and b) third formation cycle.

Batteries & Supercaps

Research Article
doi.org/10.1002/batt.202400764

Chemistry Europe
European Chemical
Societies Publishing

Table 4. Pouch cell characteristics postformation. Specific energy and energy density calculated based on a single electrode stack.

Anode in Gr/SiO‖ LFP full-cell	ICE [%]	Capacity [mAh]	Energy density [Wh L^{-1}]	Specific energy [Wh kg^{-1}]
p-f$_4$CB$_0$CNT$_{01}$	79.83	90.0	332.6	181.1
n$_4$CB$_2$CNT$_0$	90.26	103.8	370.5	200.9
f$_4$CB$_2$CNT$_0$	89.26	100.7	355.7	198.8
f$_4$CB$_1$CNT$_{01}$	89.86	103.9	361.3	204.4
f$_4$CB$_0$CNT$_{01}$	90.74	104.8	370.7	204.0
f$_3$CB$_0$CNT$_{01}$	90.82	104.8	373.2	205.4
n$_4$CB$_0$CNT$_{01}$	91.12	105.3	378.7	207.1

As a result of the lower irreversible losses of the cells with anodes containing Li–SiO, the capacity of these cells was 17% higher compared to the cells with anodes containing p-SiO (104.8 vs. 90 mAh). The specific energy of the cells with p-SiO-based anodes was 181.1 Wh kg^{-1}, whereas cells with Li–SiO-based anodes exhibited a specific energy of 205.4 Wh kg^{-1}. The energy calculation is based on a single stack comprising the anode and cathode composites, the separator, and each half of the current collector. Electrolyte and pouch foil are not considered in this calculation.

The results of the rate capability test in pouch cells, as shown in **Figure 5**, indicate generally a high discharge rate capability up to a current density of 5 mA cm^{-2} (corresponding to 2C), where the cells retained 89.7% (p-f$_4$CB$_0$CNT$_{01}$) or 88.7% (f$_4$CB$_0$CNT$_{01}$) of the nominal capacity. At higher current densities, a significant decrease in dischargeable capacity was observed. Notably, cells with p-SiO-containing anodes exhibited higher capacity

retention, which can be attributed to the thinner coating, resulting from the higher specific capacity of p-SiO compared to Li–SiO. The lower polarization at a current density of 5 mA cm^{-2}, as shown in Figure 5d, further supports this explanation.

These results contrast with the half-cell measurements, where lower polarization was observed for Li–SiO-containing electrodes. However, in the full-cell setup, the reduced thickness of the p-SiO-based electrodes appears to play a more critical role in overall cell performance. Nevertheless, the significant capacity loss during formation results in lower usable capacity for anodes comprising p-SiO (1.84 mAh cm^{-2}) compared to those with Li–SiO (2.17 mAh cm^{-2}) at 0.25 mA cm^{-2}.

The internal resistance of the cells was calculated by applying a current pulse before and after the rate capability test. As can be seen on the lefthand side of **Figure 6**b, prior to the rate capability test, the cells with p-SiO-based anodes exhibited slightly lower internal resistance but experienced a more pronounced increase during the test than the cells with Li–SiO-based electrodes. Consequently, the internal resistance of both cell types was ≈43 Ω cm^2 after the rate capability test.

Figure 6 shows the results of the cycling stability test. Cells with anodes containing Li–SiO (f$_4$CB$_0$CNT$_{01}$) displayed a significantly higher capacity of 96 mAh at the beginning of the test, compared to 80 mAh for the cells with p-SiO-based anodes (p-f$_4$CB$_0$CNT$_{01}$). After this, both cell types exhibited a similar rate of capacity fading and reached 80% of their initial capacity after ≈500 cycles. Additionally, DCIR measurements were taken every 50 cycles during the test (Figure 6b), showing that both systems underwent a comparable rise in resistance during cycling. Thus, a significant influence of the prelithiation of SiO on the cycling stability or internal resistance was not observed.
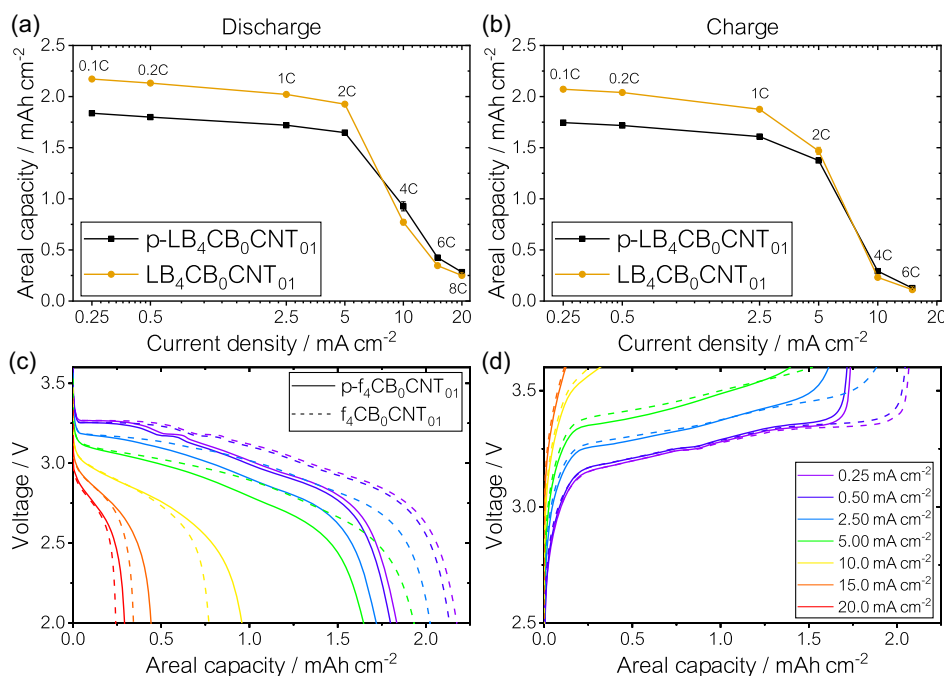

Figure 5. Rate capability test of Gr/SiO‖LFP pouch cells, with anodes consisting p-SiO (p-f$_4$CB$_0$CNT$_{01}$) or Li–SiO (f$_4$CB$_0$CNT$_{01}$); areal capacity dependent on current density during a) discharge and b) charge and voltage curves at different current densities of c) discharge and d) charge, where the solid lines represent p-f$_4$CB$_0$CNT$_{01}$ and the dashed lines represent f$_4$CB$_0$CNT$_{01}$.
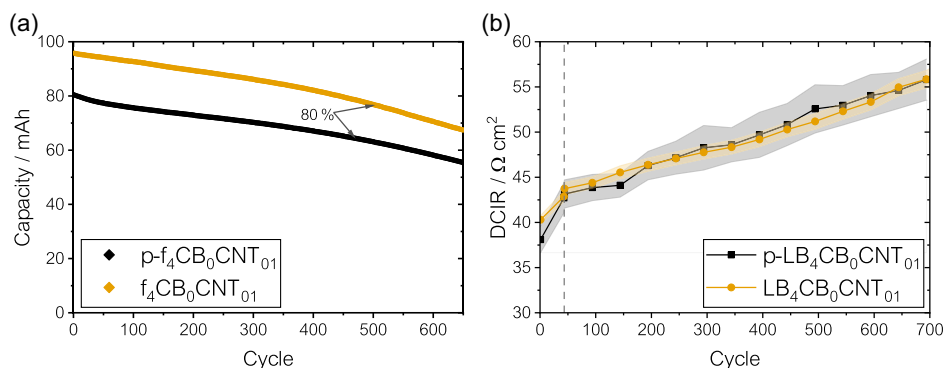
Batteries & Supercaps

Research Article
doi.org/10.1002/batt.202400764

Chemistry Europe
European Chemical
Societies Publishing

Figure 6. Cycling stability test of Gr/SiO‖LFP pouch cells with anodes consisting p-SiO (p-$f_4CB_0CNT_{01}$) or Li–SiO ($f_4CB_0CNT_{01}$); a) capacity over cycles and b) internal resistance over cycles. The shaded area represents one standard deviation around the mean, and the vertical dashed line marks the transition between the rate capability test and the cycling stability test.

3.2. Comparison of Nonfunctionalized SBR and Functionalized SBR

Functionalizing the polymeric binder presents a promising strategy to enhance the particle–binder connection's strength. Carboxyl (—COOH) groups, for instance, can establish robust interactions with Si particles via silyl ester bonds.[37] This interaction is expected to be beneficial for electrode performance and durability.[38] In this section, we compare suspensions and electrodes containing Li–SiO in combination with functionalized SBR ($f_4CB_2CNT_0$) and a nonfunctionalized SBR ($n_4CB_2CNT_0$), with CB as the only conductive additive in both formulations. Detailed information about the formulations is provided in Table 1. We investigated the influence of SBR functionalization on the rheological properties of the suspensions, the mechanical properties of the electrodes, and their electrochemical performance in half-cells and full-cells.

The rheological properties, as shown in **Figure 7**, of suspensions containing either nonfunctionalized SBR ($n_4CB_2CNT_0$) or functionalized SBR ($f_4CB_2CNT_0$) exhibited similar overall behavior. Both samples demonstrated a similar shear-thinning effect and liquid-like behavior ($G' < G''$) across nearly all frequencies. Although the suspension with the functionalized SBR ($f_4CB_2CNT_0$) exhibited slightly lower viscosity in the low shear rate range (13.3 vs. 16.3 Pa s at 1 s^{-1}) and lower structural strength at rest, these differences were not significant and could be attributed to minor variations during the mixing process. It is worth mentioning that the rheological properties of both suspensions were not optimal for large-scale coating processes because of their relatively flat viscosity curves and a liquid-like behavior at rest. This could potentially result in issues, such as sedimentation, during storage of the suspensions or separation during filtration. Addressing these challenges may require adjustments to the formulation or the mixing process.

In contrast to the rheological properties, a notable discrepancy was observed in the adhesion strength (Table 2) of the composites on the current collector. While the electrode with nonfunctionalized SBR ($n_4CB_2CNT_0$) exhibited sufficient adhesion to the substrate foil with an adhesion strength of 1.07 N mm^{-2}, this value was ≈50% lower (0.49 N mm^{-2}) when functionalized SBR ($f_4CB_2CNT_0$) was used instead. This represents a significant drawback for usual electrode production processes, as poor adhesion can lead to a loss of coating by cutting or punching the electrodes or delamination can occur during winding, unwinding, or cycling.

Figure 8 shows the first and the third formation cycle of the half-cells, and Table 3 presents the corresponding values. Figure 8 shows that, in principle, the potential curves exhibit the same shape except for smaller deviations. However, the results reveal higher irreversible losses for electrodes containing functionalized
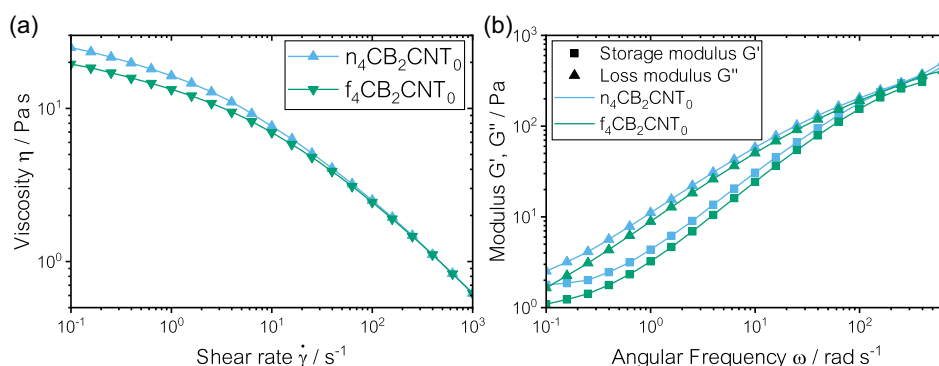

Figure 7. Rheological properties of the electrode suspensions containing either nonfunctionalized SBR ($n_4CB_2CNT_0$) or functionalized SBR ($f_4CB_2CNT_0$); a) viscosity curves and b) frequency-dependent behavior.

Batteries & Supercaps

Research Article
doi.org/10.1002/batt.202400764

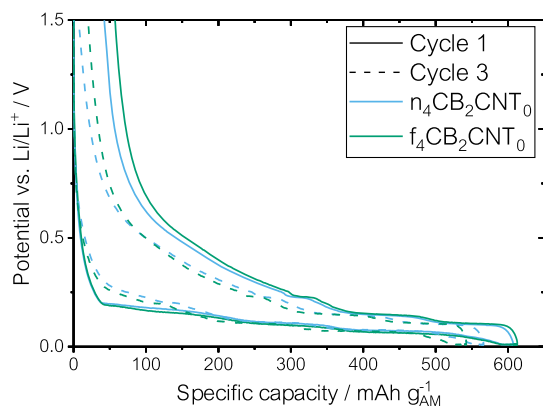**Chemistry Europe**
European Chemical
Societies Publishing

Figure 8. First formation cycles (solid lines) and third formation cycles (dashed lines) of half-cells with electrodes containing nonfunctionalized SBR ($n_4CB_2CNT_0$) and functionalized SBR ($f_4CB_2CNT_0$).

SBR (90.9% ICE) compared to the electrodes utilizing nonfunctionalized SBR (93.1% ICE). Additionally, also during the third formation cycle, the coulombic efficiency was lower in the case of the electrodes with functionalized SBR ($f_4CB_2CNT_0$), as depicted in Figure 8. Consequently, the reversible capacity with the functionalized SBR postformation was ≈ 524 mAh g^{-1}, compared to 555 mAh g^{-1} with the nonfunctionalized SBR ($n_4CB_2CNT_0$).

During the rate capability test in half-cells (**Figure 9**), electrodes containing functionalized SBR ($f_4CB_2CNT_0$) consistently exhibited lower specific capacities than the electrodes containing nonfunctionalized SBR. For instance, at a current density of 5 mA cm^{-2}, electrodes with nonfunctionalized SBR had a capacity of 484 mAh g^{-1}, whereas those with functionalized SBR reached 401 mAh g^{-1}. Additionally, the capacity retention at 10 mA cm^{-2} was lower for the electrodes with functionalized SBR (75.9%) compared to those with nonfunctionalized SBR (83.17%).

One possible reason for the lower capacities can be observed in the corresponding potential curves (Figure 9b), which show increased polarization for the electrodes with functionalized SBR. This is contradictory, as these electrodes have slightly lower mass loading, where lower polarization would typically be expected. The increased resistance may be due to the partial destruction of the electrode composite during the rate capability test, leading to a loss of contact between the active material particles. The significant capacity loss of around 20% over 16 cycles

during the rate capability test supports this explanation. In contrast, electrodes with nonfunctionalized SBR only lost around 11%. Overall, the combination of irreversible capacity loss during formation and faster capacity fading resulted in generally lower specific capacities for electrodes with functionalized SBR.

Table 4 presents the full-cell properties after formation. Similar to the half-cells, full-cells with anodes using the functionalized SBR ($f_4CB_2CNT_0$) showed higher irreversible losses compared to the cells with nonfunctionalized SBR as an anodic binder ($n_4CB_2CNT_0$). As a result, the cell capacity postformation was $\approx 3\%$ lower (100.7 mAh) compared to (103.8 mAh) cells with nonfunctionalied SBR.

The results of the rate capability test, shown in **Figure 10**, indicate a lower discharge capacity for cells with anodes containing the functionalized SBR compared to those with nonfunctionalized SBR, up to a current density of 5 mA cm^{-2}. At higher current densities, the capacities were similar, suggesting that the ionic conductivity of the electrolyte may become the limiting factor. As observed in the half-cell measurements, full-cells with functionalized SBR anodes also exhibited increased polarization during the charge rate capability test (Figure 10d), reinforcing the notion of compromised mechanical integrity in the negative electrodes.

However, during the discharge rate capability test, the decline in capacity of the cells with anodes containing the functionalized SBR was relatively modest ($<10\%$) compared to the half-cells. This could be attributed to the applied pressure on the pouch cells, which helped maintaining the electrode integrity and the contact between the particles. Nevertheless, the fading was still more pronounced than in cells with nonfunctionalized SBR anodes ($<5\%$).

The results of the cycling stability test, as shown in **Figure 11**, reveal inferior stability of cells with anodes containing functionalized SBR ($f_4CB_2CNT_0$) compared to those with nonfunctionalized SBR ($n_4CB_2CNT_0$). As depicted in Figure 11a, cells with the functionalized SBR in the anode composite displayed lower capacity values at the beginning of the test. This was due to the accelerated capacity fading the cell experienced during the preceding rate capability test. After ≈ 50 cycles, the fading rate aligned with that of the cells using a nonfunctionalized binder in the anode composite. In the long term, cells with functionalized SBR appeared to age more slowly. However, this occurred primarily after the cells had already reached their end-of-life (EoL) criterion, defined as retaining less than 80% of their initial capacity. The EoL was reached after 286 cycles for cells with anodes containing
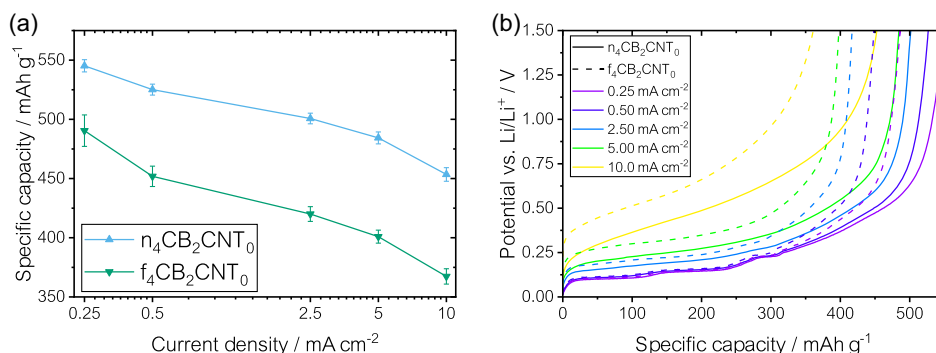

Figure 9. Potential-controlled rate capability (delithiation) test of electrodes utilizing nonfunctionalized SBR ($n_4CB_2CNT_0$) and functionalized SBR ($f_4CB_2CNT_0$) conducted in half-cells; a) capacity over current density and b) potential curves at various current densities.

Batteries & Supercaps
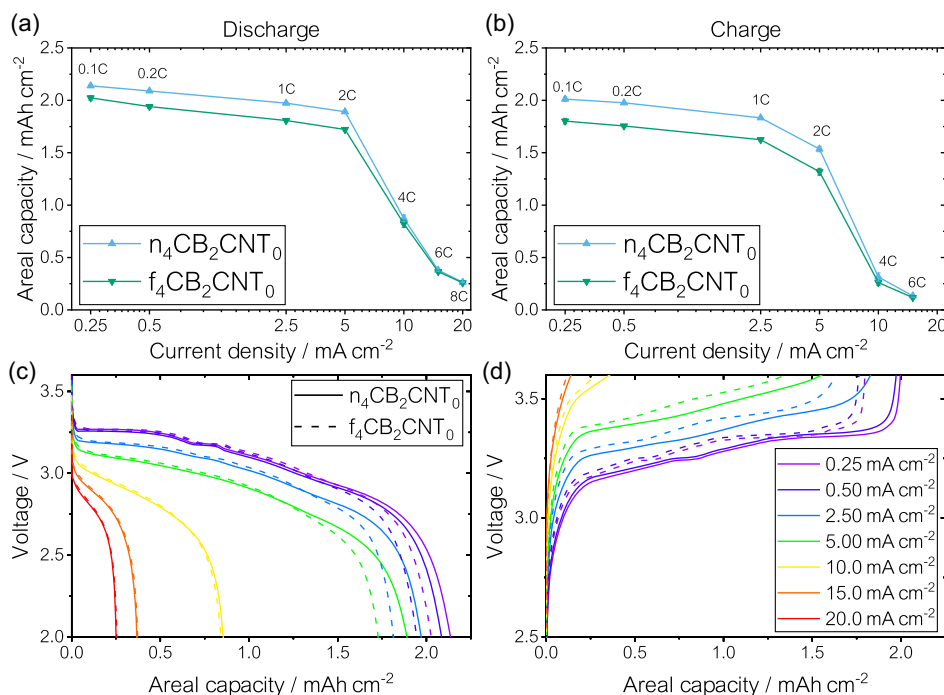
Research Article
doi.org/10.1002/batt.202400764

Chemistry Europe
European Chemical
Societies Publishing

Figure 10. Rate capability test of Gr/SiO∥LFP pouch cells with anodes consisting nonfunctionalized SBR ($n_4CB_2CNT_0$) or functionalized SBR ($n_4CB_2CNT_0$); areal capacity dependent on current density during a) discharge and b) charge and voltage curves at different current densities of c) discharge and d) charge, where the solid lines represent $n_4CB_2CNT_0$ and the dashed lines represent $f_4CB_2CNT_0$.

Figure 11. Cycling stability test of Gr/SiO∥LFP pouch cells with anodes utilizing nonfunctionalized SBR ($n_4CB_2CNT_0$) or functionalized SBR ($f_4CB_2CNT_0$); a) capacity over cycles and b) internal resistance over cycles. The shaded area represents one standard deviation around the mean and the vertical dashed line marks the transition between the rate capability test and the cycling stability test.

functionalized SBR. The cells with anodes containing nonfunctionalized SBR reached EoL after 351 cycles.

The internal resistance (Figure 11b) of cells with anodes utilizing functionalized SBR was slightly lower (41 Ω cm^2 compared to 45 Ω cm^2 after 700 cycles). However, the difference was not very pronounced, as the error bands, representing one standard deviation around the mean, overlap. Additionally, the increase in the internal resistance was similar for both cell types.

3.3. Multifunctional Role of SWCNTs

SWCNTs, recognized for their remarkable electrical and mechanical properties, have emerged as a promising additives in LIB electrodes, particularly in combination with silicon-based anodes.[11,19–21] In this section, we explore their multifaceted impact in combination with prelithiated SiO on the rheological properties of the suspensions, the mechanical properties of the electrodes, and the electrochemical cell properties in half-cells and full-cells. We compare suspensions and electrodes with the following formulations: 2 wt% CB, no SWCNTs, and functionalized SBR ($f_4CB_2CNT_0$); 1 wt% CB, 0.1 wt% SWCNTs, and functionalized SBR ($f_4CB_1CNT_{01}$); 0 wt% CB, 0.1 wt% SWCNTs, and functionalized SBR ($f_4CB_0CNT_{01}$); and 0 wt% CB, 0.1 wt% SWCNTs, and nonfunctionalized SBR ($n_4CB_0CNT_{01}$).

Detailed information about these formulations can be found in Table 1. The results of the rheological measurements are shown in **Figure 12**. It is evident that suspensions containing carbon nanotubes displayed significantly higher viscosity compared to those containing only CB. For example, the suspension
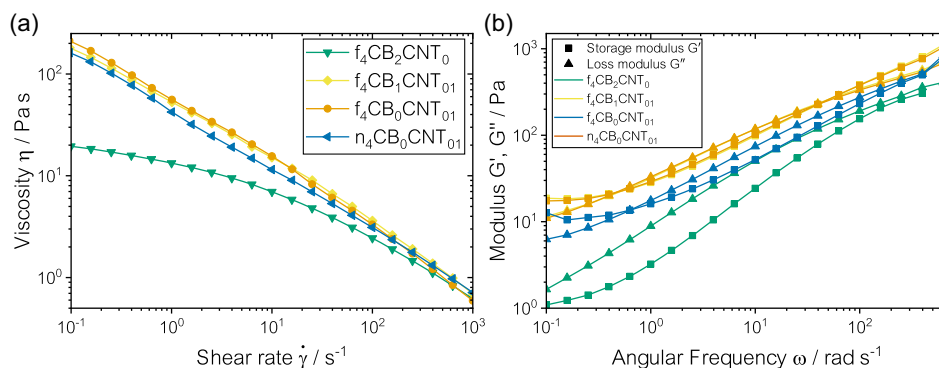
Batteries & Supercaps

Research Article
doi.org/10.1002/batt.202400764

Chemistry Europe
European Chemical
Societies Publishing

Figure 12. Rheological properties of the electrode suspensions containing as conductive additive either CB only ($f_4CB_2CNT_0$), a combination of CB and SWCNTs ($f_4CB_1CNT_{01}$), SWCNTs only ($f_4CB_0CNT_{01}$), or SWCNTs only in combination with nonfunctionalized SBR ($n_4CB_0CNT_{01}$); a) viscosity curves and b) frequency-dependent behavior.

containing only SWCNTs and no CB ($f_4CB_0CNT_{01}$) exhibited a viscosity over 300% higher than the suspension with only CB ($f_4CB_2CNT_0$) (56 vs. 13 Pa s at a shear rate of $1\ s^{-1}$). Additionally, a more pronounced shear-thinning effect was observed. Frequency analysis (Figure 12b) revealed a gel-like behavior ($G' > G''$) at rest with G' exceeding 10 Pa for the SWCNT-containing samples, which is essential for sedimentation stability. In contrast, the suspension without SWCNTs exhibited liquid-like behavior across all frequencies, making it unstable against sedimentation. The suspension with a combination of CB and SWCNTs ($f_4CB_1CNT_{01}$) showed no significant differences in rheological properties compared to the suspension with only SWCNTs in terms of both viscosity and frequency-dependent behavior.

The suspension using SWCNTs in combination with nonfunctionalized SBR showed slightly lower viscosity (42 vs. 56 Pa s at a shear rate of $1\ s^{-1}$) and a generally lower G' compared to the suspension with nonfunctionalized SBR. This suggests an improved interaction between the functionalized SBR and the carbon nanotubes. The robust shear-thinning behavior and enhanced structural strength make the suspensions-containing SWCNTs highly suitable for large-scale coating processes.

Table 2 and **Figure 13** present the adhesive strength of the electrode composites on copper foil. As shown, the electrodes

containing only SWCNTs and no CB ($f_4CB_0CNT_{01}$ and $n_4CB_0CNT_{01}$) exhibited the highest adhesive strength, 1.06 and 1.08 N mm^{-2}, respectively. In contrast, the samples using either CB alone ($f_4CB_2CNT_0$) or a combination of CB and SWCNTs ($f_4CB_1CNT_{01}$) showed adhesion values more than 50% lower, at 0.49 and 0.39 N mm^{-2}, respectively.

These results indicate that SWCNTs not only have a strong influence on the rheological properties of battery electrode suspensions but also significantly enhance the adhesive strength of the electrode composite. Replacing CB with carbon nanotubes can effectively double the tensile strength, likely because more binder is available to interact with the current collector surface rather than being adsorbed onto the surface of CB particles.

Figure 14 illustrates the first and third formation cycles of the half-cells, while Table 3 provides the measured values during formation. As shown, the electrodes with only SWCNTs as the conductive additive exhibited the lowest irreversible losses, displaying an ICE of more than 93%. In contrast, the electrode containing only CB showed the lowest ICE of 90.89%, while the electrode utilizing a combination of CB and SWCNTs had an ICE of ≈92%. The third formation cycle (Figure 14b) revealed high coulombic efficiencies of up to 99.6% for all cells with SWCNT-containing electrodes, in contrast to the cells without nanotubes, which still exhibited significant irreversible losses (3.7%) during the final formation cycle. As a result, the electrode without SWCNTs ($f_4CB_2CNT_0$) had the lowest specific capacity (523.53 mAh g^{-1}) after formation, while the electrodes containing SWCNTs demonstrated specific capacities above 560 mAh g^{-1}.

The results of the rate capability test in half-cells are shown in **Figure 15**. Electrodes containing SWCNTs generally exhibited higher specific capacities compared to those with CB as a sole conductive additive. For instance, at a current density of 5 mA cm^{-2}, SWCNT-based electrodes displayed specific capacities between 547 and 559 mAh g^{-1}, whereas CB-based electrodes only reached 401 mAh g^{-1}. This significant difference was only partially due to the lower rate capability of CB-based electrodes and was primarily attributed to their inferior stability, while cells with CB-based anodes lost ≈20% of their capacity over the 16-cycle rate capability test, and SWCNT-containing electrodes showed no capacity loss, resulting in consistently higher
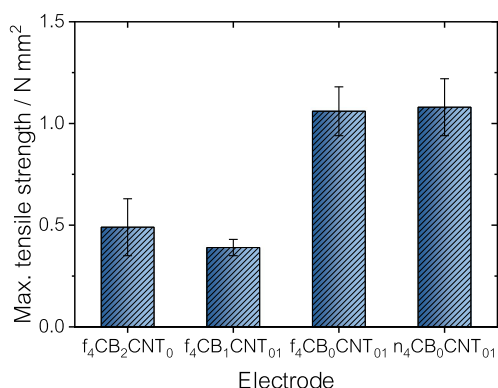

Figure 13. Adhesive strength of electrodes containing a conductive additive either CB only ($f_4CB_2CNT_0$), a combination of CB and SWCNTs ($f_4CB_1CNT_{01}$), SWCNTs only ($f_4CB_0CNT_{01}$), or SWCNTs only in combination with nonfunctionalized SBR ($n_4CB_0CNT_{01}$).
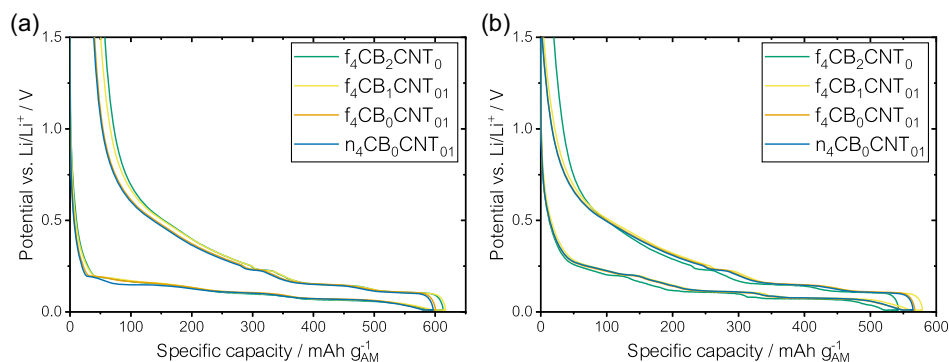
Batteries & Supercaps

Research Article
doi.org/10.1002/batt.202400764

Chemistry Europe
European Chemical
Societies Publishing

Figure 14. First formation cycle of half-cells with Li–SiO-based electrodes containing a conductive additive either CB only ($f_4CB_2CNT_0$), a combination of CB and SWCNTs ($f_4CB_1CNT_{01}$), SWCNTs only ($f_4CB_0CNT_{01}$), or SWCNTs only in combination with nonfunctionalized SBR ($n_4CB_0CNT_{01}$); a) first formation cycle and b) third formation cycle at 0.1C.

Figure 15. Potential-controlled rate capability (delithiation) test of electrodes containing a conductive additive either CB only ($f_4CB_2CNT_0$), a combination of CB and SWCNTs ($f_4CB_1CNT_{01}$), SWCNTs only ($f_4CB_0CNT_{01}$), or SWCNTs only in combination with nonfunctionalized SBR ($n_4CB_0CNT_{01}$); a) capacity over current density and b) potential curves at various current densities.

capacities. A capacity retention of over 90% was observed at a current density of 10 mA cm^{-2} ($\approx$3C) for the electrodes containing SWCNTs.

The corresponding potential curves from the rate capability test (Figure 15b) show no significant difference in polarization among the SWCNT-containing electrodes. Only at the highest current density of 10 mA cm^{-2}, a slightly higher polarization was evident in the electrodes containing 1 wt% CB and SWCNTs. Nevertheless, the specific capacity remained nearly identical across all SWCNT-containing electrode formulations. An investigation of the rate capability at even higher current densities would be of significant interest. Unfortunately, we encountered issues with internal short circuits caused by excessive dendrite growth when applying higher currents to the cells. Consequently, we limited the current density in half-cells to 10 mA cm^{-2}.

In contrast, a full-cell setup allows for the investigation of higher currents without such risks, making the evaluation of the negative electrodes in pouch cells particularly valuable.

Table 4 presents the pouch cell properties after formation, showing a trend similar to that observed in the half-cells. Lower irreversible losses were generally observed when CB was not included in the anode composite. Cells with anodes using SWCNTs as the sole conductive additive ($f_4CB_0CNT_{01}$)

exhibited an ICE of 90.74%, compared to 89.86% in cells with 1% CB ($f_4CB_1CNT_{01}$). With the use of nonfunctionalized SBR instead of functionalized SBR as the binder ($n_4CB_0CNT_{01}$), the ICE was 91.12%. In contrast, cells with CB as the sole conductive additive in the anodes ($f_4CB_2CNT_0$) showed the lowest ICE at 89.26%. Consequently, the specific energy of these cells was lower after formation (198.8 Wh kg^{-1} compared to 204 Wh kg^{-1} for cells containing only SWCNTs).

The irreversible capacity loss was generally higher in the full-cells compared to the half-cells, mainly due to the high negative-to-positive (n/p) ratio of 1.3 in the full-cell setup. This high ratio means that a significant portion of the anode's capacity is not utilized, while SEI formation still occurs across the entire electrode surface. For industry-relevant cells, a much lower n/p ratio would typically be used, which should result in lower irreversible losses, closer to the values observed in half-cells. In this research investigation, a higher ratio was chosen to reduce the risk of lithium plating during the rate capability test.

The rate capability test in pouch cells, shown in **Figure 16**, revealed only minor differences between the cells containing SWCNTs in the anodes, with all cells reached $\approx$1.9 mAh cm^{-2} at a current density of 5 mA cm^{-2}. In contrast, cells with only CB as the conductive additive ($f_4CB_2CNT_0$) reached 1.7 mAh cm^{-2} and generally exhibited lower capacities during
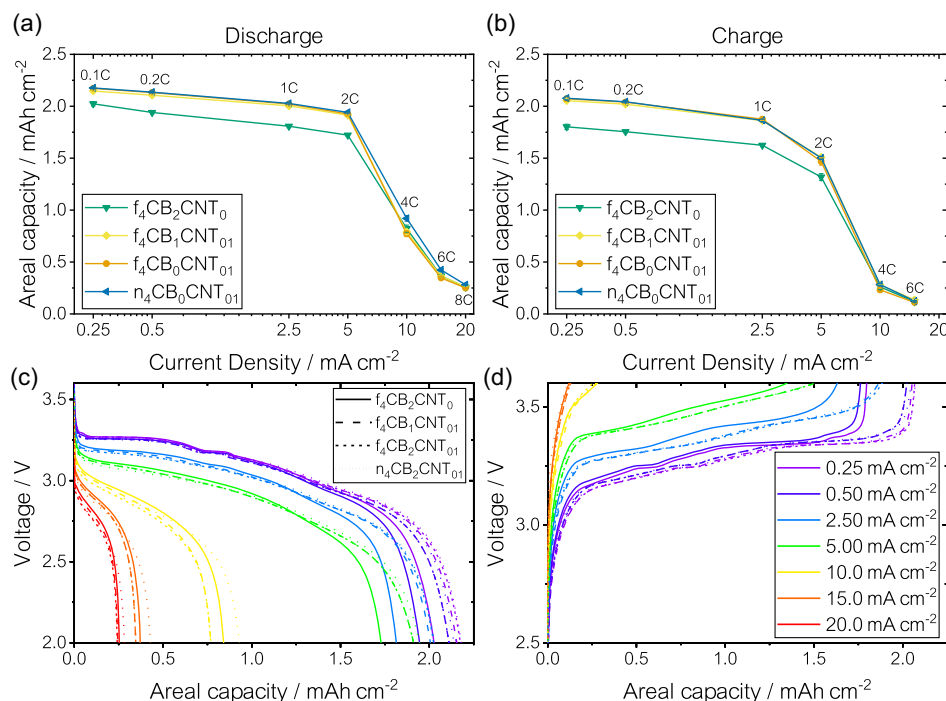
Batteries & Supercaps

Research Article
doi.org/10.1002/batt.202400764

Chemistry Europe
European Chemical
Societies Publishing

Figure 16. Rate capability test of Gr/SiO‖LFP pouch cells with anodes containing a conductive additive either CB only ($f_4CB_2CNT_0$), a combination of CB and SWCNTs ($f_4CB_1CNT_{01}$), SWCNTs only ($f_4CB_0CNT_{01}$), or SWCNTs only in combination with nonfunctionalized SBR ($n_4CB_0CNT_{01}$); areal capacity dependent on current density during a) discharge and b) charge and voltage curves at different current densities of c) discharge and d) charge.

both discharge and charge, except at higher current densities (>5 mA cm^{-2}). Furthermore, the deviation within the different cell batches was very low, as indicated by the nearly invisible error bars (representing one standard deviation around the mean) in Figure 16a,b, suggesting high and uniform electrode quality. The voltage curves (Figure 16c,d) display a very similar shape across all cells. However, during the charge rate capability test, a slightly increased polarization was noticeable in cells containing only CB and no SWCNTs in the anodes.

The results of the cycling stability test are shown in **Figure 17**. No significant differences in cycling stability between the cells with SWCNT-based anodes were observed in Figure 17a. Both capacity and capacity retention were nearly identical across

the different cell batches, with an average of ≈500 cycles to reach 80% of the initial capacity for all cells. In contrast, cells with anodes containing only CB ($f_4CB_2CNT_0$) exhibited much lower capacity and reached the EoL criterion after 286 cycles.

A drawback of the use of SWCNTs in the anode composite appears to be an increased internal resistance, as shown in Figure 17b. Cells without SWCNTs ($f_4CB_2CNT_0$) exhibited the lowest resistance values, followed by cells with 1 wt% CB and SWCNTs in the negative electrode composite ($f_4CB_1CNT_{01}$). Cells using carbon nanotubes as the sole conductive additive ($f_4CB_0CNT_{01}$ and $n_4CB_0CNT_{01}$) showed the highest internal resistance. This may be attributed to a different microstructure in the electrode composite when using SWCNTs. For instance,
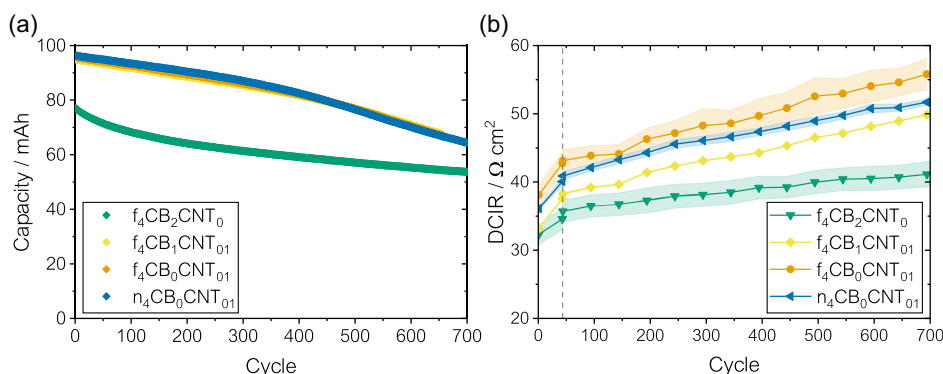

Figure 17. Cycling stability test of Gr/SiO‖LFP pouch cells with anodes containing a conductive additive either CB only (f4CB2CNT0), a combination of CB and SWCNTs (f4CB1CNT01), SWCNTs only (f4CB0CNT01), or SWCNTs only in combination with nonfunctionalized SBR (n4CB0CNT01); a) capacity over cycles and b) internal resistance over cycles. The shaded area represents one standard deviation around the mean, and the vertical dashed line marks the transition between the rate capability test and the cycling stability test.

Batteries & Supercaps

Research Article
doi.org/10.1002/batt.202400764

Chemistry Europe
European Chemical
Societies Publishing

smaller pores could result in higher diffusive resistance. However, this has not caused any negative effects in terms of rate capability or cycling stability. Nonetheless, increased resistance could pose a problem for large-format cells, such as stacked pouch cells, where higher resistance could lead to internal heat build-up, accelerating degradation. No significant differences in cycling stability or internal resistance were observed between the two different SBRs, indicating that the choice of SBR has a negligible impact on electrochemical performance when carbon nanotubes are included in the electrode formulation.

In our electrode formulations, the amount of SWCNTs was ≈ 0.4 mg per m^2 of active material surface. This is contrary to the recommendations of Kirner et al.[11] who proposed a minimum value of 1.7 mg m^{-2} for SiO-based electrodes. However, increasing the carbon nanotube content by a factor of four would not be a viable option for an electrode production process. First, SWCNTs are quite costly, and a high amount could hinder the commercialization of SiO. Second, the viscosity of the electrode suspensions would be too high for a state-of-the-art coating process due to the strong network formed by the nanotubes. This would necessitate a lower solid content in the suspensions, which would increase drying costs and potentially cause issues with the formation of the microstructure.

3.4. Increasing the Active Material Content

Increasing the active material content in electrode formulations is crucial for enhancing the overall energy density and performance of LIBs. By incorporating SWCNTs instead of CB into our electrodes, we were able to eliminate 1.75 wt% of inactive material. The active mass content can be further increased by reducing the binder content in the electrode formulation. In this section, we compare suspensions and electrodes containing Li–SiO combined with functionalized SBR and SWCNTs as additives. The binder content was either 4 wt% ($f_4CB_0CNT_{01}$) or 3 wt% ($f_4CB_0CNT_{01}$). Detailed information about the formulations is provided in Table 1. The results of the rheological measurements are shown in **Figure 18**. It is evident that a lower binder content significantly influenced the rheological properties of the electrode suspension. Due to the lower CMC content in the suspension with 3 wt% binder ($f_3CB_0CNT_{01}$), the viscosity

at a shear rate of 1 s^{-1} was nearly halved (28.9 Pa s compared to 56 Pa s) relative to the suspension with 4 wt% binder ($f_4CB_0CNT_{01}$). However, the presence of SWCNTs kept the viscosity within a suitable range for the coating process. The measurements with variable frequency (Figure 18b) showed generally lower G′ and G″ values for the suspension with 3 wt% binder compared to the one with 4 wt% binder. Despite this, the gel-like behavior in the low-frequency range was maintained, with sufficient structural strength (G′ > 10 Pa) to ensure stability against sedimentation.

Table 2 presents the adhesive strength of the electrode composites on copper foil. The electrode with 3 wt% binder had significantly lower adhesion of 0.47 N mm^{-2}, compared to 1.06 N mm^{-2} for the electrode with 4 wt% binder. The lower adhesion is a major drawback of the electrode with lower binder content, as it led to a loss of electrode composite along the edges during cutting and punching for cell assembly.

Figure 19 illustrates the first and third formation cycles of the half-cells, while Table 3 provides the measured values during formation. The binder content had minimal effect on the electrochemical properties observed during formation. The ICE of the electrode with 4 wt% binder was 91.28%, while the electrode with 3 wt% binder had a slightly higher ICE of 93.44%. Similarly, the specific capacities were nearly identical, with 567.4 mAh g^{-1} for the electrode with 4 wt% binder and 568.7 mAh g^{-1} for the
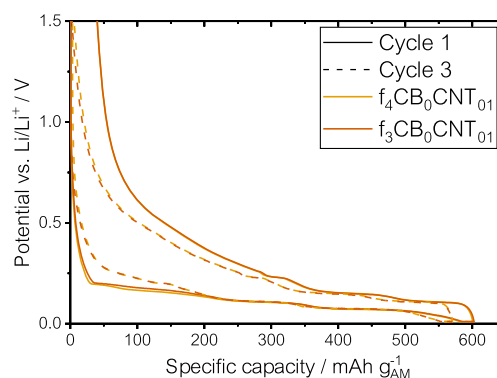
Figure 19. First formation cycles (solid lines) and third formation cycles (dashed lines) of half-cells with electrodes containing 4 wt% binder ($f_4CB_0CNT_{01}$) and 3 wt% binder ($f_3CB_0CNT_{01}$).
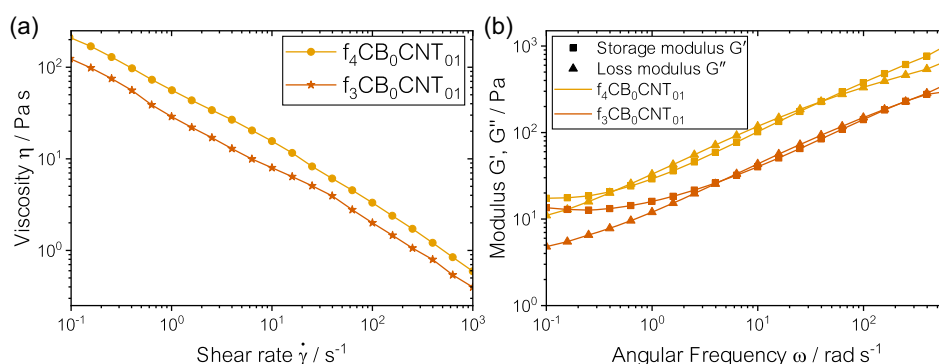
Figure 18. Rheological properties of the electrode suspensions containing either 4 wt% binder ($f_4CB_0CNT_{01}$) or 3 wt% binder ($f_3CB_0CNT_{01}$); a) viscosity curves and b) frequency-dependent behavior.

Batteries & Supercaps

Research Article
doi.org/10.1002/batt.202400764

Chemistry Europe
European Chemical
Societies Publishing

electrode with 3 wt% binder. The potential curves in Figure 19 also show nearly identical characteristics.

The results of the rate capability test in half-cells are shown in **Figure 20**. A lower rate capability was observed in electrodes with 3 wt% binder ($f_3CB_0CNT_{01}$) compared to those with 4 wt% binder ($f_4CB_0CNT_{01}$). The capacity values were generally lower, except at the lowest current density of $0.25\ mA\ cm^{-2}$. However, the discrepancy in specific capacity remained within 3%, even at the highest current density of $10\ mA\ cm^{-2}$. At this current density, the electrode with 3 wt% binder exhibited a specific capacity of $506.4\ mAh\ g^{-1}$, compared to $523.7\ mAh\ g^{-1}$ for the electrode with 4 wt% binder, corresponding to capacity retentions of 88.7–91.6%, respectively. Additionally, increased polarization in the electrodes with 3 wt% binder, noticeable even at moderate rates such as $2.5\ mA\ cm^{-2}$, is evident in the potential curves

(Figure 20b). This could be attributed to a partial loss of contact with the current collector due to poor adhesion, as previously mentioned.

The measured values from the formation of pouch cells with varying binder content in the anode composite are provided in Table 4. Both cell types exhibited similar irreversible capacity loss during formation, resulting in a capacity of 104.8 mAh for each.

The discharge rate capability in **Figure 21**a shows the areal capacity of the full-cells as a function of current density. The cells with the two different negative electrode formulations, containing either 4 wt% binder ($f_4CB_0CNT_{01}$) or 3 wt% binder ($f_3CB_0CNT_{01}$), displayed similar capacities across all tested current densities. Both cell types maintained high areal capacities of around $2.0\ mAh\ cm^{-2}$ at low current densities. However, at higher current densities ($5\ mA\ cm^{-2}$ and above), a slight divergence in
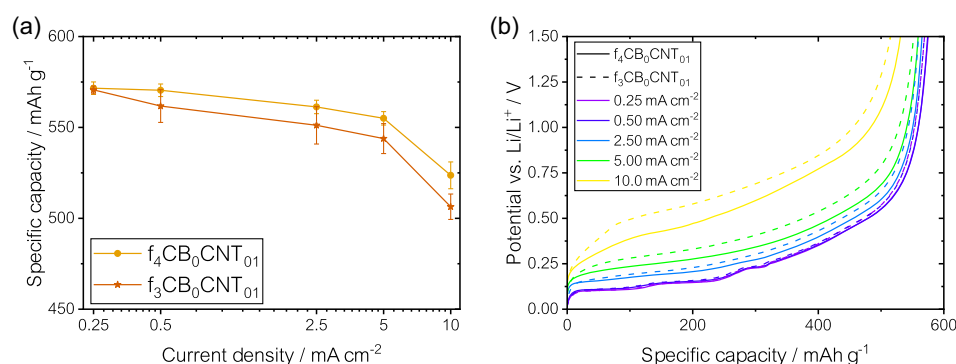

Figure 20. Potential-controlled rate capability (delithiation) test of electrodes 4 wt% binder ($f_4CB_0CNT_{01}$) or 3 wt% binder ($f_3CB_0CNT_{01}$); a) capacity over current density and b) potential curves at various current densities.
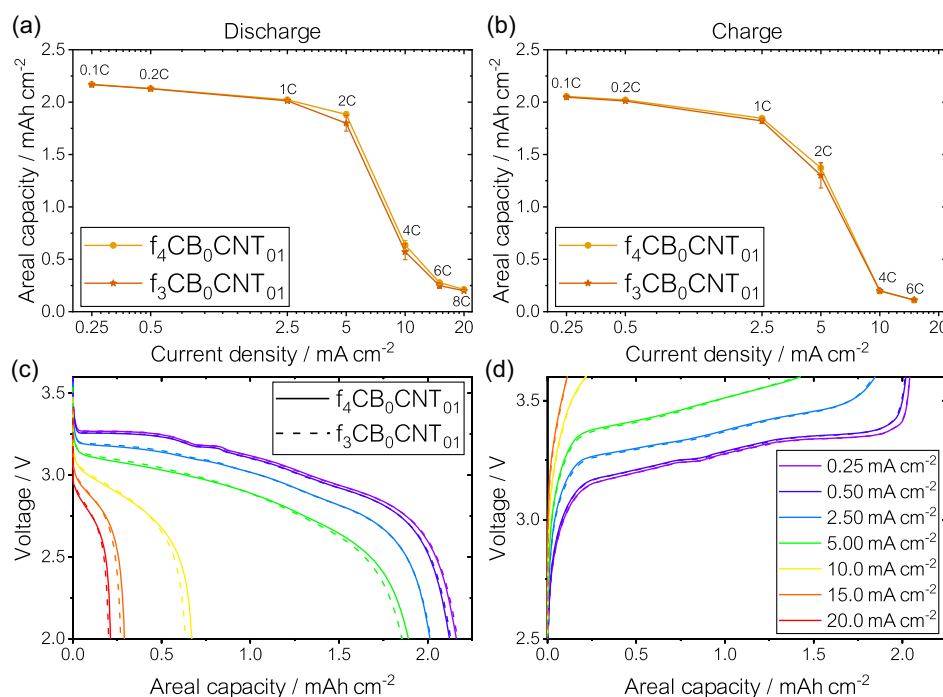

Figure 21. Rate capability test of Gr/SiO‖LFP pouch cells with anodes containing a conductive additive either 4 wt% binder ($f_4CB_0CNT_{01}$) or 3 wt% binder ($f_3CB_0CNT_{01}$); areal capacity dependent on current density during a) discharge and b) charge and voltage curves at different current densities of c) discharge and d) charge.
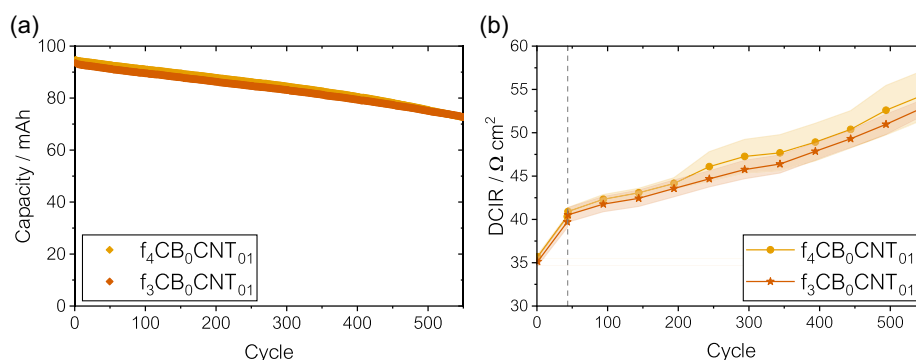
Batteries & Supercaps

Research Article
doi.org/10.1002/batt.202400764

Chemistry
Europe
European Chemical
Societies Publishing

Figure 22. a) Long-term stability test and b) trend of the internal resistance during the rate capability test and the long-term cycling. The shaded areas represent one standard deviation around the mean.

capacity retention was observed, with the cells containing 3 wt% binder showed marginally lower retention compared to those with 4 wt% binder. This indicates that the reduced binder content may negatively affect the discharge rate capability under high current densities, though the difference is minor, suggesting that even with 3 wt% binder, the performance remained sufficient at high discharge rates.

The charge rate capability (Figure 21b) follows a similar trend. Both formulations maintained high areal capacities close to 2.0 mAh cm^{-2} at low current densities of 0.25 and 0.5 mA cm^{-2}. As current density increased, the capacities decreased but the overall capacity retention remains comparable between the two cell types with different anode formulations. This suggests that reducing the binder content of the anodes to 3 wt% is a viable approach to increase the active mass content without significantly compromising the charge rate capability.

The voltage profiles during discharge (Figure 21c) and charge (Figure 21d) provide additional insights into the performance of the negative electrode formulations in the pouch cells. Both cell types exhibited similar voltage curves with no significant differences. The overlap of the curves for cells with 3 and 4 wt% binder in the anodes suggests that reducing the binder content does not significantly influence the overall voltage characteristics, aligning with the observed capacity retention.

The results of the cycling stability test are shown in **Figure 22**a. Both cell types, with different binder content in the anode composite, exhibited nearly the same capacity at the onset of the test. Subsequently, they displayed a relatively stable fading rate over 500 cycles until they reached 80% of their initial capacity with no significant deviation between the two cell types. This indicates that a low binder content of 3 wt% does not significantly affect the cycling stability of the cells.

Figure 22b shows the internal resistance throughout the rate capability test and the cycling stability test. Initially, both cell types exhibited similar internal resistance values. As cycling progressed, an increase in DCIR was observed for both systems with a slightly higher rise in the cells using anodes with 4 wt% binder. Despite this, the difference in internal resistance between the two formulations remained small, indicating that reducing the binder content does not significantly affect the internal resistance.

4. Conclusion

This study examined the effects of various anode–electrode formulations, considering different types of Si-containing active materials, the use of SWCNTs, the type and share of binder, and the share of active material itself on the rheological properties of electrode suspensions, as well as the mechanical electrode properties, and electrochemical performance of Gr/SiO negative electrodes. The findings lead to the following conclusions.

First, the use of prelithiated SiO resulted in a very high suspension pH of around 12.25, leading to degradation of CMC binder and unfavorable rheological properties. Additionally, the high pH negatively affected the mechanical properties of the electrode, particularly its adhesion to the current collector. These issues pose challenges for a large-scale production process. Despite these drawbacks in rheological and mechanical properties, the electrochemical properties of Gr/SiO-based electrodes made from Li–SiO proved promising. Compared to electrodes with p-SiO, the ICE was significantly higher and comparable to state-of-the-art graphite electrodes. With our blends containing 20% Li–SiO, an ICE of more than 91% ICE in full-cells was reached, compared to less than 80% for p-SiO-based anodes. Regarding cycling stability, no significant difference between the two types of SiO was observed.

The comparison between the functionalized and nonfunctionalized SBR in the electrode formulation revealed no significant differences in rheological suspension properties. However, electrodes with nonfunctionalized SBR exhibited significantly higher adhesion to the current collector. Additionally, these electrodes showed notably better stability in both half-cells and full-cells. Therefore, we conclude that the use of nonfunctionalized SBR is much more suitable for Li–SiO-based electrodes than functionalized SBR.

Through the incorporation of SWCNTs, we observed a significant impact on the rheological properties of the suspension. Viscosity increased by 300% at a shear rate of 1 s^{-1}, and the suspension transitioned from liquid-like to gel-like behavior at rest, which is essential for maintaining suspension stability. This shows how the robust nanotube network can partially counterbalance the adverse effects of Li–SiO on rheological properties. According to our results, the use of SWCNTs leads to improved adhesion and

Batteries & Supercaps

Research Article
doi.org/10.1002/batt.202400764

Chemistry Europe
European Chemical
Societies Publishing

can be regarded as crucial for implementing an industrial production process for electrodes based on Li–SiO. Regarding the electrochemical performance, the use of SWCNTs leads to lower irreversible losses and higher cycling stability compared to the use of CB. For instance, without SWCNT, the investigated pouch cells lost an average of 18% of their capacity over 44 cycles of rate capability testing. In contrast, adding just 0.1 wt% SWCNTs to the electrode formulation significantly improved stability with a capacity loss of less than 3%. These findings underscore the pivotal role of SWCNTs in SiO-based negative electrodes.

Furthermore, we demonstrated that the choice of binder (functionalized or nonfunctionalized SBR) had negligible effects on the electrochemical performance of the electrodes when SWCNTs were incorporated. This suggests that the binder type becomes less critical in the presence of SWCNTs, simplifying material selection for electrode formulations.

By reducing the binder content from 4 to 3 wt%, we obtained a high active mass content of 96.8%. This lower binder content resulted in a significant decrease in the viscosity and the structural strength of the suspension, along with reduced adhesion of the electrode composite to the current collector. However, an analysis of rate capability, cycling stability, and internal resistance indicates that lowering the binder content from 4 to 3 wt% is a viable strategy for increasing the active material content without significantly compromising cell performance. The cells with different shares of binder demonstrated similar rate capability and a capacity retention of ≈80% after 500 cycles, with comparable internal resistance. This underscores the robustness of the formulation with a low binder content, making it a promising approach to increase active material content, and consequently, the specific energy of Gr/SiO electrodes. However, the issue of poor adhesion must be addressed before practical application can be considered.

To summarize, Li–SiO is a promising material to be used in anodes for next-generation LIBs after practical issues for processability will be solved.

This work provides essential insights into correlations between formulations, processability, and electrochemical performance connected with the application of Li–SiO and, thus, substantially supports the development of an industrial production process.

Acknowledgements

Conflict of Interest

The authors declare no conflict of interest.

Data Availability Statement

The data that support the findings of this study are available from the corresponding author upon reasonable request.

[1] S. Bourderau, T. Brousse, D. M. Schleich, *J. Power Sources* **1999**, *81*, 233.
[2] N. Kambe, M. S. Dresselhaus, G. Dresselhaus, S. Basu, A. R. McGhie, J. E. Fischer, *Mater. Sci. Eng.* **1979**, *40*, 1.
[3] H. Wu, Y. Cui, *Nano Today* **2012**, *7*, 414.
[4] M. N. Obrovac, L. Christensen, D. B. Le, J. R. Dahn, *J. Electrochem. Soc.* **2007**, *154*, A849.
[5] K. Pan, F. Zou, M. Canova, Y. Zhu, J.-H. Kim, *J. Power Sources* **2019**, *413*, 20.
[6] Y. Reynier, C. Vincens, C. Leys, B. Amestoy, E. Mayousse, B. Chavillon, L. Blanc, E. Gutel, W. Porcher, T. Hirose, C. Matsui, *J. Power Sources* **2020**, *450*, 227699.
[7] Z. Liu, Q. Yu, Y. Zhao, R. He, M. Xu, S. Feng, S. Li, L. Zhou, L. Mai, *Chem. Soc. Rev.* **2019**, *48*, 285.
[8] a) W. Wu, Y. Liang, H. Ma, Y. Peng, H. Yang, *Electrochim. Acta* **2016**, *187*, 473; b) J. Wang, H. Zhao, J. He, C. Wang, J. Wang, *J. Power Sources* **2011**, *196*, 4811; c) M. Miyachi, H. Yamamoto, H. Kawai, T. Ohta, M. Shirakata, *J. Electrochem. Soc.* **2005**, *152*, A2089.
[9] T. Hirose, K. Takahashi, T. Matsuno, Y. Osawa, M. Furuya, R. Sakai, C. Matsui, H. Koide, *J. Electrochem. Soc.* **2020**, *167*, 120523.
[10] C.-H. Doh, C.-W. Park, H.-M. Shin, D.-H. Kim, Y.-D. Chung, S.-I. Moon, B.-S. Jin, H.-S. Kim, A. Veluchamy, *J. Power Sources* **2008**, *179*, 367.
[11] J. Kirner, Y. Qin, L. Zhang, A. Jansen, W. Lu, *J. Power Sources* **2020**, *450*, 227711.
[12] C. Meyssonnier, C. Chalard, A. Merabet, N. Goubard-Bretesché, N. Dupré, C. Paireau, B. Lestriez, *J. Electrochem. Soc.* **2024**, *171*, 70501.
[13] J. W. Choi, D. Aurbach, *Nat. Rev. Mater.* **2016**, *1*, 359.
[14] H. J. Kim, S. Choi, S. J. Lee, M. W. Seo, J. G. Lee, E. Deniz, Y. J. Lee, E. K. Kim, J. W. Choi, *Nano Lett.* **2016**, *16*, 282.
[15] B. Huang, T. Huang, L. Wan, A. Yu, *ACS Sustainable Chem. Eng.* **2021**, *9*, 648.
[16] A. Cholewinski, P. Si, M. Uceda, M. Pope, B. Zhao, *Polymers* **2021**, *13*, 631.
[17] a) D. Bresser, D. Buchholz, A. Moretti, A. Varzi, S. Passerini, *Energy Environ. Sci.* **2018**, *11*, 3096; b) S. Lim, S. Kim, K. H. Ahn, S. J. Lee, *J. Power Sources* **2015**, *299*, 221; c) V. Scheck, M. Memm, M. Hölzle, M. Wohlfahrt-Mehrens, *J. Electrochem. Soc.* **2023**, *170*, 120514.
[18] X. Lu, G. J. Lian, J. Parker, R. Ge, M. K. Sadan, R. M. Smith, D. Cumming, *J. Power Sources* **2024**, *592*, 233916.
[19] S.-H. Park, P. J. King, R. Tian, C. S. Boland, J. Coelho, C. Zhang, P. McBean, N. McEvoy, M. P. Kremer, D. Daly, J. N. Coleman, V. Nicolosi, *Nat Energy* **2019**, *4*, 560.
[20] W. Kang, Q. Zhang, Y. Jia, X. Liu, N. Jiang, Y. Zhao, C. Wu, L. Guan, *J. Power Sources* **2024**, *602*, 234338.
[21] Z. He, Z. Xiao, H. Yue, Y. Jiang, M. Zhao, Y. Zhu, C. Yu, Z. Zhu, F. Lu, H. Jiang, C. Zhang, F. Wei, *Adv. Funct. Mater.* **2023**, *33*, 2300094.
[22] P. Haberzettl, N. Filipovic, D. Vrankovic, N. Willenbacher, *Batteries* **2023**, *9*, 581.
[23] a) X. Feng, J. Yang, X. Yu, J. Wang, Y. Nuli, *J. Solid State Electrochem.* **2013**, *17*, 2461; b) Y. Xiong, H. Xing, Y. Fan, Y. Wei, J. Shang, Y. Chen, J. Yan, *RSC Adv.* **2021**, *11*, 7801; c) S. Komaba, K. Shimomura, N. Yabuuchi, T. Ozeki, H. Yui, K. Konno, *J. Phys. Chem. C* **2011**, *115*, 13487.
[24] J. Song, Z. Feng, Y. Wang, X. Zhou, X. Zhang, K. Wang, J. Xie, *Solid State Ionics* **2019**, *343*, 115070.
[25] K. Urban, G. Wagner, D. Schaffner, J. Ulrich, *Chem. Eng. Res. Des.* **2006**, *84*, 1081.
[26] J. Sato, V. Breedveld, *Appl. Rheol.* **2005**, *15*, 390.
[27] T. G. Mezger, *The Rheology Handbook*, Vincentz Network, Hannover **2014**.
[28] W. Haselrieder, B. Westphal, H. Bockholt, S. Diener, A. Höft, A. Kwade, *Int. J. Adhes. Adhes.* **2015**, *60*, 1.
[29] D. B. Braun, M. R. Rosen, *Rheology Modifiers. Practical Use and Applilcation*, Willlam Andrew Publishing, Norwich **1999**.
[30] H. Meeuw, V. K. Wisniewski, B. Fiedler, *Polymers* **2018**, *10*, 999.
[31] T. A. Osswald, N. Rupolph, *Polymer Rheology Fundamentals and Applications*, Hanser Fachbuchverlag, Munich **2014**.
[32] J. M. Krishnan, A. P. Deshpande, P. B. S. Kumar, *Rheology of Complex Fluids*, Springer, New York, NY **2010**.

[33] C. Kuo, H. Hsu, C. Lan, *J. Power Sources* **2023**, *558*, 232599.

[34] C. G. Lopez, R. H. Colby, J. T. Cabral, *Macromolecules* **2018**, *51*, 3165.

[35] C. G. Lopez, W. Richtering, *Carbohydr. Polym.* **2021**, *267*, 118117.

[36] T. Hirose, M. Morishita, H. Yoshitake, T. Sakai, *Solid State Ionics* **2017**, *304*, 1.

[37] a) F. Jeschull, F. Scott, S. Trabesinger, *J. Power Sources* **2019**, *431*, 63; b) T. R. Martin, R. T. Pekarek, J. E. Coyle, M. C. Schulze, N. R. Neale, *J. Mater. Chem. A* **2021**, *9*, 21929.

[38] J. Hu, Y. Wang, D. Li, Y.-T. Cheng, *J. Power Sources* **2018**, *397*, 223.